Elucidating the local structure of V substitutes in In_2S_3 as potential intermediate band material by x-ray absorption spectroscopy and first principles calculations

Journal of Physics: Energy

PAPER

Elucidating the local structure of V substitutes in In_2S_3 as potential intermediate band material by x-ray absorption spectroscopy and first principles calculations

Elaheh Ghorbani[1], Martin Schiller[2,3], Hans H Falk[2], Leonard A Wägele[3], Stefanie Eckner[2], Francesco d'Acapito[4], Roland Scheer[3], Karsten Albe[1] and Claudia S Schnohr[2,*]

[1] Fachgebiet Materialmodellierung, Institut für Materialwissenschaft, TU Darmstadt, 64287 Darmstadt, Germany
[2] Felix-Bloch-Institut für Festkörperphysik, Universität Leipzig, Linnéstraße 5, 04103 Leipzig, Germany
[3] Martin-Luther-Universität Halle-Wittenberg, Institut für Physik, 06099 Halle, Germany
[4] CNR-IOM-OGG c/o ESRF LISA CRG, 71 Avenue des Martyrs, 38043 Grenoble, France
* Author to whom any correspondence should be addressed.

E-mail: claudia.schnohr@physik.uni-leipzig.de

Keywords: In_2S_3, indium sulphide, vanadium, local structure, thin films, x-ray absorption spectroscopy, *ab initio* calculations

OPEN ACCESS

RECEIVED
20 January 2023

REVISED
25 May 2023

ACCEPTED FOR PUBLICATION
26 May 2023

PUBLISHED
6 June 2023

Abstract

Vanadium doped indium sulphide, In_2S_3:V, is studied as a potential absorber material for intermediate band (IB) solar cells. Based on electronic considerations, it is usually assumed that V occupies octahedrally coordinated In sites, although geometrical considerations would favour tetrahedral In sites. In this study, we therefore combined experimental x-ray diffraction and x-ray absorption spectroscopy with *ab initio* theoretical calculations of both α and β phase to elucidate the incorporation of V in In_2S_3:V thin films grown with different V content and different growth temperatures. Comparing shape and position of the measured and calculated x-ray absorption edge of V, comparing experimentally determined and calculated V–S bond lengths, and evaluating the calculated heat of solution of V on different lattice sites all indicate that V is incorporated on octahedral rather than tetrahedral sites in the In_2S_3 matrix. For this material system, the electronic benefit of octahedral coordination thus outweighs the mechanical stress of the associated lattice relaxation. Finally, we studied the electronic structure of V-substituted α-In_2S_3 using hybrid density functional calculations and find that for a concentration of 1.9 at %, V on octahedrally coordinated In sites forms an empty IB isolated from valence band and conduction band (CB). By increasing the V content to 3.8 at %, however, the gap between IB and CB closes, which results in a reduction of the band gap. This differs from the electronic structure calculated for β-In_2S_3:V and clearly demonstrates that both crystal structure and V incorporation site affect the resulting electronic material properties.

1. Introduction

In the quest for high-efficiency photovoltaic devices, intermediate band (IB) solar cells have been proposed as a promising route to overcome the efficiency limits of single junction solar cells [1, 2]. The presence of a partially filled electronic band between the valence band (VB) and the conduction band (CB) of the semiconductor could provide an increased photo current due to the absorption of photons with energies lower than the band gap while at the same time maintaining the high output voltage associated with this band gap. The conversion efficiency of an optimum IB solar cell is predicted to be 63% or 46% under ideal concentration or one-Sun illumination, respectively, compared to 41% or 30% for an optimum single junction solar cell [3, 4]. In reality, efficiencies might be lower due to non-radiative multi-phonon recombination [5, 6] and overlapping absorption coefficients [7].

Significant and promising efforts have been made to realise IB solar cells [1, 2]. One route proposed to create suitable IB materials is hyper-doping of semiconductors. In particular, In_2S_3 substituted with

transition metals, In_2S_3:TM, has been identified as a most promising candidate [8]. The crystal structure of In_2S_3 can be described as a defect spinel-type structure, in which In occupies octahedrally and tetrahedrally coordinated lattice sites [9]. First principles calculations based on density functional theory (DFT) with local or semi-local approximations predict a partially filled IB for In_2S_3:V, In_2S_3:Ti and In_2S_3:Fe [8, 10]. Experimentally, In_2S_3:V [11–17], In_2S_3:Fe [10] and In_2S_3:Nb [18] have been studied. Some of the earlier works report the formation of a partially filled IB based on additional sub band gap absorption and transitions [10, 11, 18]. In contrast, some of the more recent studies find evidence that the IB formed upon transition metal substitution is in fact completely filled [13, 14, 17]. In good agreement with these findings, recent DFT based *ab-initio* calculations using the screened hybrid functional by Heyd, Scuseria, and Ernzerhof (HSE) reveal the formation of a completely filled IB for In_2S_3:V, In_2S_3:Ti and In_2S_3:Nb [19, 20]. In contrast, an empty IB is predicted theoretically for Ti and V doped In_2S_3 with an alternative trigonal crystal structure [21].

Typically, it is assumed that the transition metal ions substitute the octahedrally coordinated In sites, because transition metals are known to favour octahedral coordination [8, 19]. In fact, the calculated formation energies for In_2S_3:Fe [10], In_2S_3:Ti and In_2S_3:Nb [20] are lower for incorporation on octahedral sites than on tetrahedral sites. However, in most cases the bond lengths in octahedrally coordinated transition metal sulphides are significantly shorter than the In–S bond lengths of the octahedral lattice sites in In_2S_3. For example, the average V–S bond lengths in V_3S_4 and V_5S_8 equals 2.40 Å [22, 23], whereas the average In–S bond lengths of the octahedral sites amounts to 2.63 Å [9]. It is well known from numerous semiconductor systems that bonds tend to conserve their natural lengths upon doping or alloying [24, 25] and indeed the calculated average V–S bond length for In_2S_3:V with V incorporated on octahedral lattice sites is reported as 2.47 and 2.49 Å [8, 19]. Incorporation of V on octahedral lattice sites in In_2S_3 therefore requires strong local lattice distortions. In contrast, the average In–S bond lengths of the tetrahedral sites amounts to only 2.46 Å [9]. Incorporation on tetrahedral lattice sites would thus only slightly perturb the crystalline matrix and would thus significantly reduce the distortion energy. A similar competition between electronic and geometrical aspects was indeed already observed for doping of $CuInSe_2$ with different alkali elements, for which light alkalis prefer to substitute monovalent Cu in bulk $CuInSe_2$, whereas heavy alkalis like Cs favour incorporation on trivalent In sites [26]. Therefore, it is not known *a priori* if V is incorporated on octahedral or tetrahedral lattice sites in real In_2S_3:V material.

The prior reports on In_2S_3:V have all *presumed* that V goes on octahedral lattice sites but this issue has not been questioned in the literature. In the present study, we therefore perform a rigorous analysis of vanadium substitution in In_2S_3 thin films using x-ray diffraction (XRD) and x-ray absorption spectroscopy (XAS) measurements together with theoretical calculations. The aim of this work is to unfold whether V is incorporated on octahedral or tetrahedral lattice sites or both. While XRD provides information about the overall crystal structure, XAS yields element-specific local structural parameters such as the average bond length of a particular element in the sample. To complete the picture, DFT-based *ab-initio* calculations using the HSE hybrid functional provide bond lengths, electronic structure and heat of solutions for V incorporated on tetrahedral and octahedral lattice sites in the In_2S_3 matrix.

The paper is organised as follows: first, we describe the experimental and computational methodology used in the paper. XRD is used for the crystallographic analysis of the V-containing samples and the experimental lattice constants are compared to the values obtained by HSE calculations. Next, the analysis of the local environment surrounding the V atoms is presented using XAS data and then bond lengths are directly compared to the theoretical calculations, where we present V–S bond lengths in both α and β phases, when V is incorporated on tetrahedral and octahedral sites. Then, we analyse the energetics of V incorporation on tetrahedral and octahedral lattice sites, by calculating the heat of solution of V in, both, α and β phases. Finally, we calculate the electronic structure of α-In_2S_3:V using hybrid DFT, thus completing this comprehensive study of V substitution and the resulting effects on the electronic properties of In_2S_3 thin films.

2. Experimental details

2.1. Thin film fabrication

Polycrystalline In_2S_3 thin films containing vanadium were grown on borofloat glass by co-evaporation [15]. Borofloat glass was chosen as substrate since it is chemically and mechanically more stable than standard glass. Furthermore, it has a low Na content, which is desirable since Na incorporation is known to significantly affect the properties of In_2S_3 thin films [27–30]. Indium (6N) and sulphur (5N) were provided by thermal evaporation sources while vanadium (3N) was provided by an electron beam evaporator. The temperature-dependent elemental fluxes were determined using a quartz crystal microbalance and the thin film thickness was monitored during growth by laser-light scattering. A high sulphur flux ensured S-rich

Table 1. In_2S_3:V thin films grown at different substrate temperatures T and with different V contents. The uncertainty for the composition equals ±0.4 at % for V and In and ±0.6 at % for S.

Sample	T (°C)	V (at %)	In (at %)	S (at %)
T3ref	500	—	40.0	60.0
T3C1	500	1.9	38.6	59.5
T3C2	500	3.3	37.7	59.0
T3C3	500	5.3	35.6	59.1
T2C3	400	5.7	35.4	58.9
T1C3	300	5.9	34.7	59.4

growth conditions and the substrate temperature, as measured by a thermocouple on the back of the sample, was varied between 300 °C and 500 °C. A list of all samples and their growth temperature is given in table 1.

The In_2S_3:V thin films were grown to be ∼1 μm thick and featured a compact morphology with large grains up to approximately 1 μm in size for a growth temperature of 500 °C, as revealed by scanning electron microscopy. Decreasing the growth temperature to 300 °C significantly reduced the average grain size without affecting the overall compact morphology. The elemental composition of the thin films was determined by energy-dispersive x-ray analysis and is summarised in table 1. For the In_2S_3:V samples grown at 500 °C (T3C1, T3C2 and T3C3), the V content increases from ∼2 to ∼5 at %, representing a concentration series. The samples grown at varying temperature (T3C3, T2C3 and T1C3) all feature a V content between 5 and 6 at % and thus represent a temperature series.

2.2. XRD measurements and analysis

XRD measurements of the as-grown In_2S_3:V thin films were performed at room temperature in Bragg–Brentano geometry with a PANanalytical Empyrean using a Cu K_α source. The diffractograms were analysed using the PDXL2 software from Rigaku. After adjusting the background, all peaks were fitted simultaneously using either Pearson profiles in case of highly crystalline samples with dominating Lorentz shape or pseudo-Voigt profiles in case of samples with lower crystal quality and hence a larger Gaussian component. Lattice constants were then deduced from the peak positions assuming either a cubic or a tetragonal structure while the full width at half maximum (FWHM) of the peaks was taken as a measure for the crystallinity of the material. No indication for the presence of secondary phases was observed for any of the samples.

2.3. XAS measurements and analysis

XAS measurements were performed in fluorescence mode at the V K-edge at the LISA CRG Beamline (BM08) of the European Synchrotron (ESRF) in Grenoble, France [31]. To that end, the In_2S_3:V thin films had to be removed from the substrate since titanium traces in the glass would have led to the overlap of Ti K_β fluorescence with the V K_α signal. Therefore, 1.3 cm^2 of thin film were scraped off for each sample using blades cleaved from a silicon wafer to avoid any Ti contamination. The material was then mixed with high purity graphite in a ball mill and pressed into pellets with 8 mm diameter. The XAS spectra were recorded at room temperature using a 12-element Ge detector. A vanadium reference foil was measured simultaneously in transmission mode to enable a precise alignment of the energy scales of different spectra.

The XAS data were processed and analysed using the IFEFFIT code [32] and the corresponding user interfaces ATHENA and ARTEMIS [33]. The spectra were first aligned in energy using the measured reference foil and then normalised. The threshold energy E_0 was chosen as half-height of the absorption edge for each sample. For the analysis of the extended x-ray absorption fine structure (EXAFS), the background was subtracted and the spectra were Fourier transformed over a photo electron wave number of $k = 2.5 - 8.0$ Å^{-1} using a Hanning window with a tapering parameter of d$k = 2$ Å^{-1}. The nearest neighbour scattering contribution was then fitted over a radial range of $R = 1.0 - 3.0$ Å, applying multiple k-weights of 1, 2 and 3. Phase shifts and scattering amplitudes were calculated using FEFF9 [34]. To that end, two different structural models were applied: (i) V coordinated tetrahedrally with four S atoms and (ii) V coordinated octahedrally with six S atoms. In contrast to diffraction methods, EXAFS is a local probe and mostly measures the one-dimensional interatomic distance distribution. In most cases, the nearest neighbour signal is not affected by scattering contributions of higher neighbour shells and can be analysed independently. Indeed, for Cu-(In,Ga)-Se samples with different compositions and crystal structures, a simplified nearest neighbour model and cluster models based on 35 atoms and different crystal structures yielded the same structural parameters within the uncertainty [35]. Therefore, the two nearest neighbour models mentioned above were chosen for In_2S_3:V, representing V on tetrahedral and octahedral lattice sites, respectively.

The difference in threshold energy, ΔE_0, and the amplitude reduction factor, S_0^2, were set to a common value for all samples, leaving the average bond length R and the bond length variation σ^2 as fitting parameters. Note that fitting the coordination number N is not feasible in this case due to the strong correlation between N and σ^2 and the relatively small usable k-range of the data. Furthermore, a reliable deduction of coordination numbers requires the measurement of a suitable reference compound under the same experimental conditions, which was not possible in the current study because vanadium sulphides very quickly oxidise. A direct estimation of the V–S coordination number from a fit of the EXAFS data is thus not feasible in the present case. Fits based on the bond valence model [36] (establishing a link between N and R) yield the same R values within uncertainty, the same trends for σ^2 as reported below and a coordination number of roughly 5.5. The latter would support octahedral coordination even if this is derived from R rather than fitted independently. The overall uncertainty of the results for R and σ^2 was estimated by systematic tests of all settings applied during the analysis, including background subtraction, Fourier transformation and choice of ΔE_0. Both structural models yield fitting results that are identical within this uncertainty. Therefore, these first nearest neighbour structural parameters do not depend on the assumption of tetrahedral or octahedral coordination in the initial structural model.

Using FEFF9, the x-ray absorption near edge structure (XANES) was also calculated. The XANES is sensitive to the local coordination and three-dimensional structure also beyond the nearest neighbour shell. Therefore, individual calculations were performed for each sample, taking into account the structural parameters determined by XRD and EXAFS and assuming different lattice sites for V incorporation as explained in detail further below.

3. Computational details

Calculations in the framework of DFT were carried out using the Vienna *ab-initio* simulation package [37, 38]. Calculations were performed for unit cells containing 53 and 80 atoms in cubic α-In_2S_3 and tetragonal β-In_2S_3, respectively. The results were obtained using the HSE screened hybrid functional [39]. The contribution of Hartree–Fock exchange, α, was set to the standard value of 0.25 and the screening range of the electron interaction was treated by adjusting the Thomas–Fermi screening parameter, w, to 0.13 $Å^{-1}$, as successfully applied in our previous studies [40]. The interactions between the ionic cores and the valence electrons were described with the projector augmented-wave approach [41, 42]. The semi-core 3 *p*, 4 *s*, and 3 *d* states of V were treated as part of the valence. The wave functions were expanded up to a cut-off energy of 400 eV and the Brillouin zone was sampled using a $2 \times 2 \times 2$ k-point mesh for α-In_2S_3 and a $4 \times 4 \times 1$ k-point mesh for β-In_2S_3. In all calculations the spin polarisation effects were taken into account. The convergence thresholds for electronic self-consistency and residual Hellmann–Feynman force component on each atom were set to 10^{-5} eV and 0.05 eV $Å^{-1}$, respectively. Both, the ionic positions and the cell metric, were allowed to relax.

4. Results and discussions

4.1. Crystallographic structure

In_2S_3 crystallises in a defect spinel-type structure, where the S atoms form a closed-packed lattice [9, 20]. While the octahedrally coordinated metal sites are fully occupied by In, one third of the tetrahedrally coordinated metal sites are vacant. In the room temperature β-phase, these vacancies exhibit long-range ordering, leading to a distortion of the cubic symmetry and thus to a tetragonal structure with three nonequivalent In sites, namely octahedral 16h, octahedral 8c and tetrahedral 8e plus the tetrahedral vacancies. In contrast, the high-temperature α-phase features a random distribution of the vacancies across the tetrahedral sites and thus exhibits a cubic structure with two nonequivalent In sites, namely octahedral 16d and tetrahedral 8a, which also includes the tetrahedral vacancies.

Detailed analysis of the pure In_2S_3 thin film grown at 500 °C (T3ref) using XRD, glancing incidence wide angle XRD and Raman scattering confirmed that the sample crystallised in the tetragonal β-phase as expected for stoichiometric material. In contrast, the In_2S_3:V thin films with ∼2 at % V or more exhibit the cubic α-phase, in good agreement with previous studies on In_2S_3:Fe [10]. No secondary phases are observed experimentally.

The lattice constant and FWHM obtained from the XRD analysis are shown in figure 1. The FWHM was evaluated for the 222 peak of the α-phase or the 206 peak of the β-phase for In_2S_3:V and In_2S_3, respectively. As shown in figure 1(a), the FWHM for the sample grown at 500 °C with the lowest V content (T3C1) is only slightly larger than that of the pure In_2S_3 reference. With increasing V content and decreasing growth temperature, the FWHM significantly increases, reaching more than four times the value of the pure In_2S_3 reference and three times the value of T3C1 for the sample grown at 300 °C with ∼6 at % V (T1C3). This

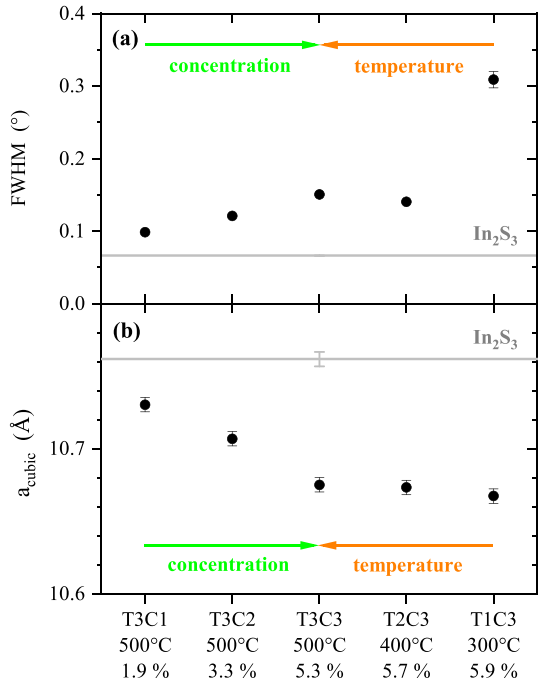

Figure 1. Crystal structure parameters for In_2S_3:V thin films determined by XRD. (a) Full width at half maximum (FWHM) of the α-222/β-206 diffraction peak occurring at $2\theta = 28.7^\circ$ and (b) cubic lattice constant a_{cubic} for samples with different V content and different growth temperature. The grey lines represent the corresponding values for the pure In_2S_3 reference grown at 500 °C.

Table 2. The HSE calculated lattice constant (in Å) of pure and V-doped α-In_2S_3.

pure α-In_2S_3	$In_{20}S_{32}$:V_1^{16d}	$In_{20}S_{32}$:V_1^{8a}	$In_{19}S_{32}$:V_2^{16d}	$In_{19}S_{32}$:V_2^{8a}
10.83	10.81	10.80	10.78	10.76

clearly indicates a diminishing crystallinity with increasing V content and decreasing growth temperature. Similar results were also obtained for In_2S_3:V thin films grown with varying V content at 300 °C [15].

The cubic lattice constant a_{cubic} is plotted in figure 1(b). Note that a representative cubic lattice constant can also be deduced for pure In_2S_3 via the relation $3a_{cubic}^3 = 2a_{tet}^2 c_{tet}$, with a_{tet} and c_{tet} being the lattice constants of the tetragonal β-phase. The resulting value of $a_{cubic} = 10.762$ Å is only slightly smaller than the corresponding value of $a_{cubic} = 10.782$ Å obtained from the tetragonal lattice constants given in [9]. As can be seen in figure 1(b), the lattice constant strongly decreases with increasing V content. Similar observations have been reported for In_2S_3:V, In_2S_3:Fe, In_2S_3:Nb and In_2S_3:Ti from both experimental studies and theoretical calculations [10, 15, 17–20]. The reduction of the lattice constant and hence the unit cell volume is caused by the incorporation of the smaller transition metal atoms on the In lattice sites. Substitutional incorporation of V is further supported by the decrease of the In concentration with increasing V content as shown in table 1, leading to a constant metal concentration between 40 and 41 at %. Interestingly, the lattice constant is not significantly affected by the growth temperature, demonstrating that the latter clearly affects the crystalline quality of the material but not the dimension of the crystal lattice itself.

Table 2 shows the theoretically calculated lattice constant of pure and V-doped α-In_2S_3, where V ions are incorporated on 16d octahedral and 8a tetrahedral sites. As described above, incorporation of V into In_2S_3 takes it from the tetragonal β-phase to the cubic α-phase. In contrast to β-In_2S_3, where the In vacancies are ordered, in α-In_2S_3 the In vacancies are randomly distributed all over the existing tetrahedral sites. This gives rise to 56 different configurations of the calculated unit cell with various orderings of the In vacancies. First, we used the functional by Perdew, Burke, and Ernzerhof (PBE) to calculate the total energy of all 56 configurations and identified the lowest energy configuration. Due to the high computational cost of the HSE functional, all our α-phase calculations were performed for this lowest energy configuration of the α-In_2S_3. The HSE lattice constants thus calculated are reported in table 2. The atomic size of In (1.55 Å) is larger than that of V (1.35 Å). Hence, as expected and in agreement with the experimental results of figure 1(b), incorporation of V in the system leads to the decrease of lattice size. This decrease seems to be slightly more pronounced for V ions substituting 16d octahedral sites than 8a tetrahedral sites. In all cases, the calculated lattice constants are somewhat larger than the measured ones if the absolute values are considered. However,

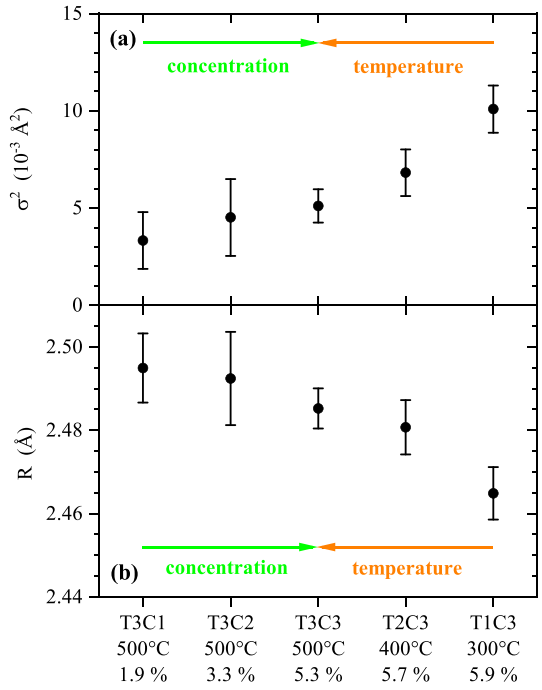

Figure 2. (a) V–S bond length variation σ^2 and (b) average bond length R determined from the EXAFS analysis for In_2S_3:V thin films.

compared to pure In_2S_3, the measured lattice constants decrease by 0.03 $\pm$ 0.01 Å and 0.05 $\pm$ 0.01 Å, respectively, for samples grown at 500 °C with 1.9 and 3.3 at % V (T3C1 and T3C2). Similarly, compared to pure In_2S_3, the calculated lattice constants decrease by 0.02 to 0.03 Å and by 0.05 to 0.07 Å, respectively, for $In_{20}S_{32}$:V_1 (corresponding to 1.9 at % V) and $In_{19}S_{32}$:V_2 (corresponding to 3.8 at % V). Thus, the measured and calculated relative changes of the lattice constant upon V incorporation match very well.

4.2. Local structure

Analysis of the EXAFS data yields the mean value (average bond length R) and the variance (bond length variation σ^2) of the V–S interatomic distance distribution as plotted in figure 2. The bond length variation is a measure for both structural (static) and thermal (vibrational) disorder in the V–S bonds. Since all measurements were performed at the same temperature, differences in σ^2 between the different samples should mostly be connected to differences in structural disorder. For thin films grown at 500 °C, the σ^2 values given in figure 2(a) slightly increase with increasing V content and although the differences are within the experimental uncertainty the trend is systematic and fits well to that of the FWHM shown in figure 1(a). The bond length variation further increases with decreasing growth temperature, reaching a value for the sample grown at 300 °C with ∼6 at % V (T1C3) that is a factor of three larger than σ^2 of the sample grown at 500 °C with ∼2 at % V (T3C1), which is again in excellent agreement with the FWHM obtained from XRD measurements. The diminishing crystallinity of the material with increasing V content and decreasing growth temperature thus corresponds to an increasing variation of the V–S bond lengths and hence to an increase of structural disorder on the sub-nanometer scale.

The average bond length R falls between 2.46 and 2.50 Å for all samples as shown in figure 2(b). This is larger than the average V–S bond lengths of ∼2.40 Å in different vanadium sulphides [22, 23], it agrees relatively well with the average In–S bond length of 2.46–2.47 Å of the tetrahedral sites in In_2S_3 and it is significantly smaller than the average In–S bond length of 2.60–2.64 Å of the octahedral sites in In_2S_3 [9]. It is in excellent agreement though with the calculated *relaxed* V–S bond length of 2.49 Å for V atoms incorporated on the octahedral 16h and 8c sites of β-In_2S_3 [19]. No calculations have yet been reported for the relaxed V–S bond length on tetrahedral sites in β-In_2S_3 or for either octahedral or tetrahedral sites in α-In_2S_3. The average V–S bond length plotted in figure 2(b) further exhibits a continuous decrease with increasing V content and decreasing growth temperature. For the concentration series grown at 500 °C, this matches very well with the decrease in cubic lattice constant shown in figure 1(b). Indeed, when comparing the sample with ∼5 at % V (T3C3) with the sample with ∼2 at % V (T3C1), a_{cubic} decreases by 0.5% while R decreases by 0.4%. This corresponds to a change of 0.15% and 0.12% per at % V. The similarity of the decrease in a_{cubic} and R is somewhat unusual, though. For many semiconductor alloy systems the relative

Table 3. The HSE calculated In–S and V–S average bond lengths (in Å) in pure In_2S_3 and V-doped In_2S_3. For pure In_2S_3, the average experimental bond lengths are given in parentheses [9].

	In_2S_3		In_2S_3:V			
	In^{oct}–S	In^{tet}–S	In^{oct}–S	In^{tet}–S	V^{oct}–S	V^{tet}–S
α-In_2S_3	2.64 (2.64)	2.50 (2.47)	2.64	2.50	2.44	2.24
β-In_2S_3	2.64 (2.63)	2.50 (2.46)	2.64	2.50	2.50	2.35

change of the element-specific bond length is about an order of magnitude smaller than the relative change in lattice constants. For ternary III-V and II–VI zincblende alloys, for instance, the change of the element-specific bond lengths amounts to only ∼20% of the change of the respective lattice site distance [24]. For I-III-VI_2 chalcopyrite alloys and I_2-II-IV-VI_4 kesterite alloys, the element-specific bond lengths change even less, corresponding to only ∼10% of the change expected based on the lattice constants [24, 25, 35]. This characteristic behaviour originates from the fact that stretching or compressing the bonds requires significantly more energy than bending the bonds. Therefore, the lattice mismatch in many alloy systems is accommodated mostly by bond angle relaxation and only to a small extent by bond length relaxation [24]. Here, the change of the V–S bond length corresponds to ∼80% of the change expected based on the lattice constant. This indicates a different energy balance between bond length relaxation and bond angle relaxation for V incorporation in In_2S_3 compared to other semiconductor alloy systems. Most interestingly, the average V–S bond length also decreases with decreasing growth temperature although the lattice constant in this case remains nearly unchanged as seen in figures 1(b) and 2(b). A potential explanation could be the diminishing crystalline quality and the concomitant increase of structural disorder with decreasing growth temperature. This could lead to a reduction of the strain exercised by the In_2S_3 matrix on the V–S bonds, which therefore change even more towards the typical values observed for pure vanadium sulphides.

In table 3, we present the HSE calculated average bond lengths of the pure and V-incorporated α-In_2S_3 as well as those of the pure and V-incorporated β-In_2S_3. The bond lengths are reported for both octahedral and tetrahedral sites. Obviously, the average In–S bond length for a given coordination is the same in α and β phase of pure In_2S_3. In contrast, it varies significantly for tetrahedral and octahedral sites. This is in excellent agreement with the experimental results reported in [9], which correspond to an average In–S bond length of ∼2.63 Å and ∼2.46 Å for octahedral and tetrahedral lattice sites, respectively, in both α-In_2S_3 and β-In_2S_3. Note that the values for the α phase in table 3 were obtained by estimating the cubic lattice constant at room temperature either from the tetragonal lattice constants or by extrapolating the temperature dependence of the cubic lattice constant to 300 K, which both give the same result. The calculated bond lengths are slightly larger than the experimental ones in good agreement with the slightly larger lattice constant as discussed above. More importantly, however, the average In–S bond lengths do not change upon V incorporation into either α-In_2S_3 or β-In_2S_3 although the lattice constant clearly decreases for In_2S_3:V. Hence, the latter effect originates solely from the strong local lattice relaxation around the V atoms as seen in table 3. For inclusion of V on In octahedral sites, the V–S bond length relaxes to 2.44 Å in α-In_2S_3:V and to 2.50 Å in β-In_2S_3:V compared to the In–S bond length of 2.64 Å. The same trend applies for inclusion of V on In tetrahedral sites, where the V–S bond length relaxes to 2.24 Å in α-In_2S_3:V and to 2.35 Å in β-In_2S_3:V compared to the In–S bond length of 2.50 Å. Remarkably, the calculated V–S bond lengths match the measured V–S bond lengths shown in figure 2(b) very well for V incorporated on octahedral sites whereas they are considerably smaller for V incorporated on tetrahedral sites. Thus, a comparison between experimental data and computational data for the average V–S bond length clearly indicates the inclusion of V on octahedral sites.

The XANES of the absorption spectrum contains additional information about the electronic structure and three-dimensional local geometry surrounding the V atoms. The measured spectra for all In_2S_3:V samples are shown in figure 3. Clearly, the XANES is very similar in all cases, confirming that the V atoms have a very similar local environment in all five samples. The correlation between the XANES and single electronic or structural parameters is, however, not trivial. Instead, the edge position and shape depend on coordination number, symmetry, bond length and valence state together [43–45]. To gain further insight, theoretical XANES spectra were calculated for the V K-edge of α-phase In_2S_3:V using FEFF9 [34]. A cluster of ∼200 atoms surrounding a central absorbing V was created based on cubic α-In_2S_3 with an arbitrary distribution of vacancies and V atoms incorporated on either tetrahedral (8a) or octahedral (16d) lattice sites. The calculation was performed without additional experimental broadening but with S_0^2 set to 0.7 or 0.47 for tetrahedral or octahedral coordination, respectively, to match the experimental NS_0^2 of approximately 2.8. To account for the random distribution of vacancies and V atoms, ten different clusters with different distributions were created and the resulting calculated spectra were merged to represent the average of different local configurations. As expected, the lattice constant and the V–S nearest neighbour

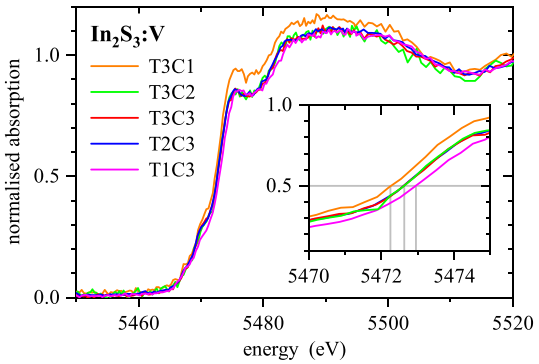

Figure 3. XANES spectra of In_2S_3:V thin films measured at the V K-edge. The inset plots the upper part of the absorption edge on an enlarged scale.

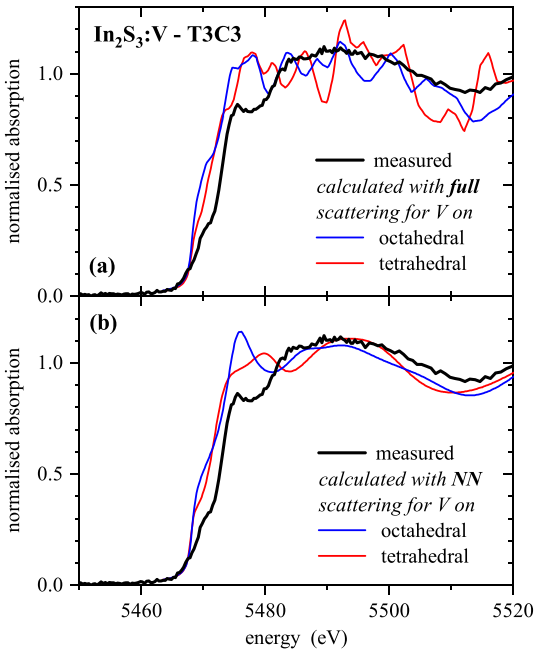

Figure 4. XANES spectrum measured at the V K-edge for the In_2S_3:V sample grown at 500 °C with ∼5 at % V (T3C3) together with the XANES spectra calculated for V incorporation on 16d octahedral or 8a tetrahedral lattice sites of α-In_2S_3 considering (a) scattering from all atoms in the cluster or (b) scattering from nearest neighbour (NN) atoms only.

distance affect the shape and edge position of the calculated XANES spectra. Therefore, separate calculations were performed for each sample with the same set of clusters but with the lattice constant and the V–S bond length adjusted to the individual values obtained from XRD and EXAFS, respectively.

As an example, figure 4 shows the measured and calculated spectra for the In_2S_3:V sample grown at 500 °C with ∼5 at % V (T3C3). In a first set of calculations, scattering of the photo electron wave from all atoms in the simulated cluster was considered. As can be seen in figure 4(a), both calculated spectra agree reasonably well with the measured spectrum in the edge region. In particular, none of them exhibits a white line or a pre-edge peak as observed for many transition metal compounds [44, 45]. Instead, the measured spectrum features a shoulder in the lower absorption edge, which is also observed for the calculated spectra, in particular for octahedral coordination of the V atoms. Note that a discrepancy in the height of spectral features is not unusual for this kind of calculations. Above the absorption edge, however, both calculated spectra show a number of narrow oscillations that are clearly not visible in the measured spectrum. Most likely, experimental broadening, static disorder in the material and thermal vibrations of the atoms prevent coherent scattering from beyond the nearest neighbour shell and thus dampen out these oscillations in the measured spectrum. Therefore, a second set of calculations was performed considering only scattering from nearest neighbour S atoms. As can be seen in figure 4(b), the calculated spectra now show the same broad feature as the measured spectrum and the fine oscillations observed in figure 4(a) have vanished. This confirms our hypothesis that structural and thermal disorder in the material prevent coherent scattering

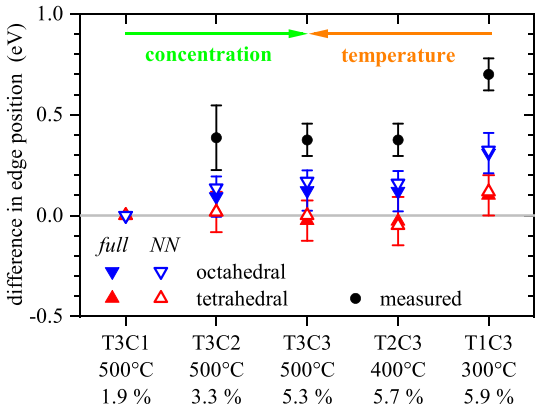

Figure 5. Shift of the edge position with respect to the In_2S_3:V sample grown at 500 °C with ∼2 at % V (T3C1) for the measured spectra (black circles) and for the spectra calculated with V incorporated on 16d octahedral sites (blue triangles) or 8a tetrahedral sites (red triangles) of α-In_2S_3 considering scattering from all atoms in the cluster (full symbols) or from nearest neighbour (NN) atoms only (open symbols).

from beyond the nearest neighbour shell. Again, the spectrum calculated for V on the octahedral site resembles the qualitative features of the absorption edge slightly better than the spectrum calculated for V on the tetrahedral site (see figure 4(b)). A similar behaviour is also observed for the other In_2S_3:V samples.

The measured XANES spectra exhibit a small shift of the edge position as shown in the inset of figure 3. To quantify this shift, the energy, at which the normalised absorption equals 0.5, was evaluated. The difference of this energy with respect to that of sample T3C1 is plotted for all In_2S_3:V samples in figure 5. Clearly, the edge position shifts to higher energy with increasing V content and decreasing growth temperature. This matches, at least qualitatively, the change of the average V–S bond length shown in figure 2(b), because a decrease of the nearest neighbour distance typically leads to a shift of the absorption edge towards higher energies [43]. The change in edge position has also been evaluated for the calculated XANES spectra (see figure 5). Obviously, considering scattering from all atoms in the cluster or from nearest neighbour atoms only does not significantly affect the shift of the edge position. For V incorporated on the tetrahedral sites, the shift is zero for all samples except the one grown at 300 °C with ∼6 at % V (T1C3), for which the edge is shifted by 0.1 ± 0.1 eV. Tetrahedral coordination thus yields a basically constant edge position of the calculated spectra. In contrast, the edge position clearly shifts to higher energy with increasing V content and decreasing growth temperature for the spectra calculated assuming V incorporation on the octahedral sites. Although the absolute shift is significantly smaller than for the measured spectra, the qualitative trend is reproduced quite well. The shape of the x-ray absorption edge and the change in its energetic position thus both indicate a predominantly octahedral coordination of the V atoms in these In_2S_3:V thin films.

4.3. Heat of solution

In order to evaluate the thermodynamic energy cost for substitution of V ions on octahedral and tetrahedral sites, we calculated the heat of solution of V on both sites using the equations:

$$\begin{aligned} H_s &= E_{In_{21-n}S_{32}:V_n} - E_{In_2S_3} - n\mu_V + n\mu_{In} \qquad (\text{for}\,\alpha - In_2S_3), \\ H_s &= E_{In_{32-n}S_{48}:V_n} - E_{In_2S_3} - n\mu_V + n\mu_{In} \qquad (\text{for}\,\beta - In_2S_3). \end{aligned} \tag{1}$$

$E_{In_{21-n}S_{32}:V_n}$ and $E_{In_{32-n}S_{48}:V_n}$ denote the total energy of the defective cell containing various concentrations of V, respectively in α- and β-phase. n is the total number of V (In) atoms added (removed) from the system. The term $E_{In_2S_3}$ accounts for the total energy of the pure α-In_2S_3 and β-In_2S_3 cells. The chemical potential of the incorporated V (substituted In) is given by $\mu_V = \mu_V^{ref} + \Delta\mu_V$ ($\mu_{In} = \mu_{In}^{ref} + \Delta\mu_{In}$), where μ_V^{ref} (μ_{In}^{ref}) is the total energy of the atom in its ground-state elemental phase, and $\Delta\mu_V$ ($\Delta\mu_{In}$) is the change in the chemical potential of the V (In), when forming the compound of interest with respect to the chemical potential of its elemental phase. Here, we considered S-rich growth condition, which is a common practice in experiments, and the formation of V was limited by the formation of the VS_4 secondary phase.

Figure 6 shows the obtained heat of solution of V in α- and β-In_2S_3, when incorporated on octahedral and tetrahedral sites under S-rich growth condition. If we first consider β-In_2S_3, substituting one octahedral In site with a V ion (corresponding to a concentration of 1.25 at %) yields a heat of solution of 0.51 eV. By increasing the number of V ions in the system to two (corresponding to a concentration of 2.5 at %), the heat

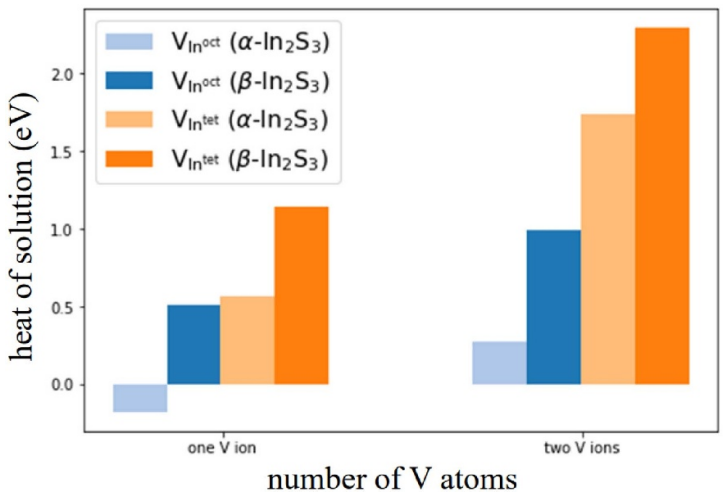

Figure 6. The HSE calculated heat of solution of V as a function of concentration under S-rich growth condition.

of solution almost doubles to 0.98 eV. Similarly, the heat of solution is 1.14 and 2.30 eV for incorporating one or two V, respectively, on tetrahedral In sites. This proportionality is observed up to four V ions (corresponding to a concentration of 5 at %, not shown). The heat of solution thus exhibits a linear dependence on the V content, demonstrating that there is no significant interaction (neither reducing nor increasing the total energy) between the V ions in β-In_2S_3 for this concentration range.

The situation is clearly different in α-In_2S_3. For substitution of octahedral In sites, the heat of solution is -0.18 eV for one V ion (corresponding to a concentration of 1.9 at %) but 0.28 eV for two V ions (corresponding to a concentration of 3.8 at %). Incorporating one or two V ions on tetrahedral In sites yields a heat of solution of 0.57 and 1.74 eV, respectively. Increasing the concentration of V from 1.9 at % to 3.8 at % thus changes the heat of solution from negative to positive for octahedral coordination and triples rather than doubles it for tetrahedral coordination. Note that both distant and close configurations of the two V ions were considered in the calculations. These findings indicate that V ions are easily incorporated on octahedral In sites in the α-phase and that for lower concentrations their inclusion occurs spontaneously without requiring energy from the environment. At the same time, the strong increase of the heat of solution for two V ions compared to one renders the formation of secondary phases very unlikely. The latter may change at higher V concentrations, though, as phase separation was reported from an experimental study for V concentrations of 7.5 at % or higher [17].

A comparison between α- and β-phase shows that the heat of solution is lower in α-In_2S_3 than in β-In_2S_3 for any given In site and V concentration. Note that the V concentration is higher in α-In_2S_3 than in β-In_2S_3 for the same number of V atoms due to the different size of the unit cell. This indicates that substitution of In sites with V is energetically less costly in the α-phase than in the β-phase. It can be understood in view of the fact that the β-phase holds a higher degree of ordering compared to the α-phase and, consequently, distorting its internal lattice through V incorporation would be energetically more expensive. For V concentrations in the range considered here, the α-phase is thus energetically favoured in agreement with experimental observations.

A comparison between octahedral and tetrahedral sites clearly shows that the heat of solution is substantially lower for V incorporation on octahedral In sites than on tetrahedral In sites for any given V concentration in both α-In_2S_3 and β-In_2S_3. The substitution of one octahedral In site in the unit cell of α-In_2S_3 even results in a negative heat of solution, as already discussed above. Hence, despite the significant local lattice distortion, V ions still prefer an octahedral rather than a tetrahedral coordination and corresponding crystal field. The calculated heat of solutions therefore clearly imply incorporation of V ions on octahedral In sites of the In_2S_3 matrix.

4.4. Electronic structure

Figure 7 shows HSE spin-polarised densities of states of V-substituted α-In_2S_3. The incorporated V^{3+} ions are added on In 16d octahedral and 8a tetrahedral sites. In the octahedral geometry of the α-In_2S_3, the six neighbouring S atoms are oriented along the $x-$, $y-$ and $z-$axis. Therefore, according to the crystal field theory, the d_{z^2} and $d_{x^2-y^2}$ orbitals of the V experience higher repulsion and are consequently pushed to higher energy levels (also known as *e* orbitals). On the other hand, the d_{xy}, d_{yz} and d_{xz} planar orbitals

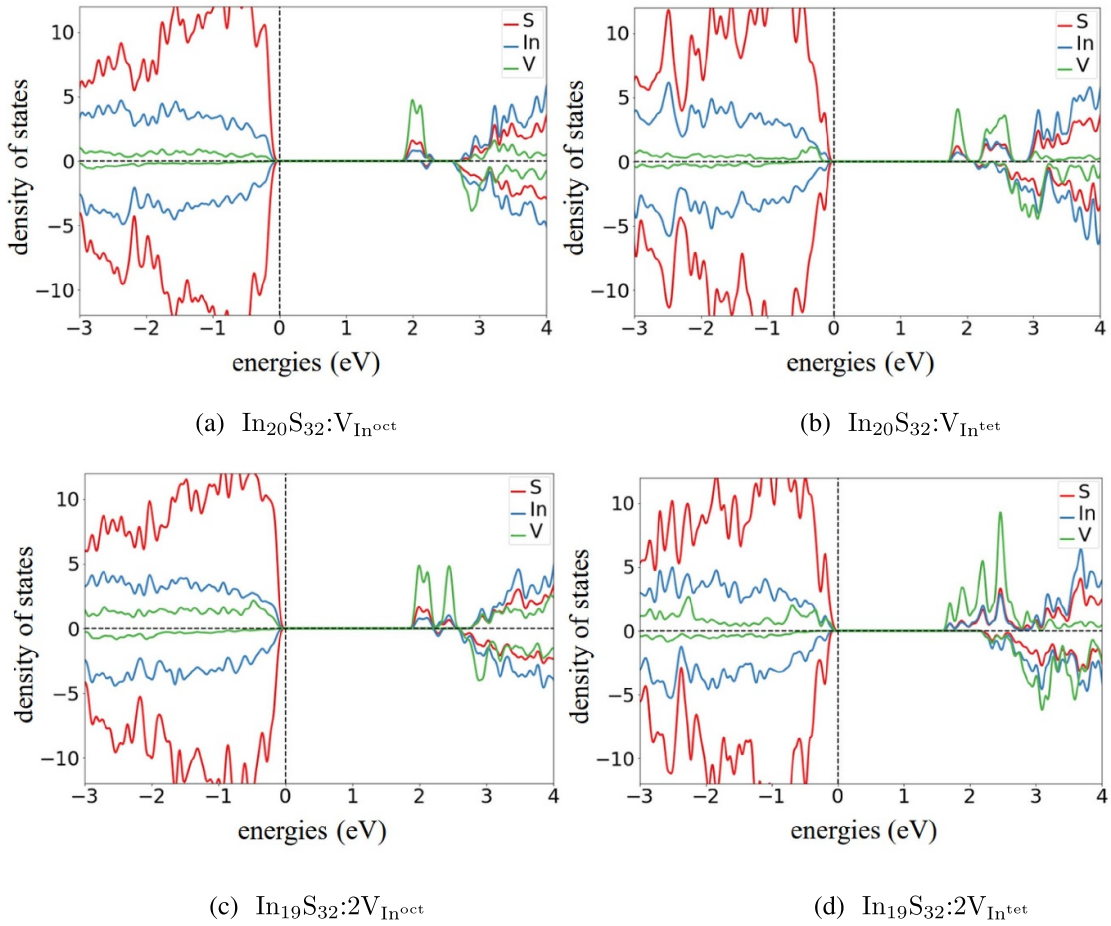

Figure 7. Spin-polarised elemental densities of states (DOS) computed for V-substituted α-In_2S_3, when V is added on 16d octahedral and 8a tetrahedral sites, in two different concentrations. Figures (a) and (b) correspond to the DOS of $In_{20}S_{32}:V_{In^{oct}}$ and $In_{20}S_{32}:V_{In^{tet}}$, respectively. Figures (c) and (d) correspond to the DOS of $In_{19}S_{32}:2V_{In^{oct}}$ and $In_{19}S_{32}:2V_{In^{tet}}$, respectively. Zero of energy corresponds to the highest occupied state.

experience lower repulsion and are pushed into lower energy levels (also known as *t* orbitals). In the tetrahedral geometry, the ligand atoms are between the crystal axes. Therefore, the d_{xy}, d_{yz} and d_{xz} planar orbitals of V interact more strongly with the S atoms than the d_{z^2} and $d_{x^2-y^2}$ orbitals. Therefore, for V on tetrahedral site, the doubly occupied *e* orbitals are pushed to lower energy levels and the empty triplet *t* orbitals are pulled to higher energy levels.

Here, we considered two concentrations of V: 1.9 at % and 3.8 at %, corresponding to the incorporation of one and two V ions in the lattice matrix, respectively. The energy level of zero corresponds to the highest occupied state. We see from figure 7 that the VB is dominated by S (3 *p*) and In (4 *d*) orbitals while the *d* orbitals of V show large hybridisation with In and S empty states in the CB. In $In_{20}S_{32}$: V_1^{oct} (figure 7(a)), one V ion substitutes In octahedral site and the *d* orbital splitting results in formation of empty in-gap states. Upon substitution of V^{3+} on In octahedral site, two electrons occupy three degenerate *t* states. This electron degeneracy generates a Jahn–Teller distortion. In consequence, the *t* state splits into doubly-occupied and singly-unoccupied sub-levels. The fully occupied lower energy branch goes to the VB and the empty higher energy branch resides inside the band gap. This empty in-gap state has a width of 0.44 eV and is separated from the VB and CB by 1.82 and 0.34 eV, respectively. Therefore, this in-gap state allows VB–IB transitions of 1.82 eV and subsequently the IB–CB transitions of 0.34 eV. Note that since the IB is fully unoccupied, the simultaneous VB–IB and IB–CB transitions cannot be achieved. Instead, due to the narrow width of the IB and small coupling between V *d* state and the host ions, the introduced IB may act as an undesired deep defect level. By adding two V ions to the system, as shown in figure 7(c), the in-gap state is not isolated from the CB anymore. In this case, the empty singlet appears below the CB and attached to it, which reduces the band gap to 1.84 eV.

Previous *ab initio* calculations using HSE functional in β-In_2S_3 revealed that incorporation of V^{3+} on In octahedral site does not result in an IB state. Instead, the partially filled *t* orbital splits into occupied and unoccupied levels inside the host bands for both low and high V concentrations of 1.25 at % and 5 at %,

respectively [19]. The origin of this qualitatively different behaviour between V^{3+} in α- and β-phases can be traced back to different crystal fields of the two phases. However, the formation of an empty IB was also reported for V-substituted In_2S_3 with a trigonal crystal structure [21].

For substitution of V on In^{tet} tetrahedral site, we see a different situation. Here, for both concentrations of 1.9 and 3.8 at %, the empty *d* orbitals of V appear higher in the band gap, as CB tails and decrease the band gap to only 1.69 and 1.17 eV for 1.9 and 3.8 at % concentrations, respectively. In the tetrahedral geometry, the *e* orbitals are below the *t* orbitals. Thus, substitution of V^{3+} on In tetrahedral site results in a doubly occupied *e* state and the triply empty *t* states. Hence, in tetrahedral geometry, there is no orbital degeneracy to be removed and consequently there exists no Jahn–Teller active centre.

5. Conclusions

In this study, we performed a combined experimental and *ab-initio* investigation of the V incorporation in In_2S_3. XRD was used to determine the crystallographic structure of In_2S_3:V thin films grown with different V content and different growth temperatures, while XAS was applied to investigate the local structure surrounding the V atoms. DFT was used to calculate lattice constants, In–S and V–S bond lengths, heat of solutions of V and the electronic structure for α- and β-phase In_2S_3:V.

Regarding the crystal structure, both XRD and DFT data confirm a decrease of the lattice constant upon inclusion of V in the system. Furthermore, the FWHM of the measured XRD data indicates a decreasing crystallinity of the material with increasing V content and decreasing growth temperature. Regarding the local structure of V in In_2S_3:V, EXAFS analysis provided the average V–S bond length and the variance of the V–S interatomic distance distribution. The average V–S bond lengths fall between 2.46 and 2.50 Å for all samples, which is in excellent agreement with the calculated V–S bond lengths for V atoms substituting the octahedral sites of α- or β-In_2S_3. The increase of the variance of the V–S distance distribution with increasing V content and decreasing growth temperature reveals that the diminishing crystallinity of the material is concomitant with increasing structural disorder also on the atomic scale. Additional information about the local geometry surrounding the V atoms was derived from a comparison of measured and calculated XANES spectra for the V K-edge of α-In_2S_3:V. The broad, washed-out features of the measured spectra above the edge suggest that the disorder in the thin films is sufficient to prevent significant coherent scattering from beyond the nearest neighbour shell. The features of the edge itself are slightly better represented by the spectra calculated for V on octahedral sites than those for V on tetrahedral sites. Similarly, the small shift in edge position with increasing V content and decreasing growth temperature is reproduced, at least qualitatively, for octahedrally coordinated V but not for tetrahedrally coordinated V.

Furthermore, we calculated the heat of solution of V for both tetrahedral and octahedral lattice sites in α-In_2S_3 and β-In_2S_3. In both cases, the heat of solution is lower for the octahedral site than for the tetrahedral site, indicating that V atoms prefer to occupy the octahedral sites and not the tetrahedral ones. Bringing together all results, we conclude that V is incorporated in In_2S_3 predominantly on octahedral In sites. For V-doped In_2S_3, the electronic benefit of octahedral coordination thus indeed dominates over the relaxation induced mechanical stress associated with incorporation on a geometrically less suitable site. This validates the results of previous reports, which assumed V to be located on octahedral lattice sites in the In_2S_3 matrix. It also highlights the electronic benefit of coordination number and symmetry as dominating factor for determining the local bonding configuration. In contrast, the relaxation induced distortion energy becomes the dominating factor for $CuInSe_2$ doped with heavy alkalis, where Cs occupies trivalent In sites rather than monovalent Cu sites in the bulk of the material [26]. In this case, however, both potential sites (Cu and In) feature tetrahedral coordination, different to the present study of In_2S_3:V.

Finally, we studied the electronic structure of the V-substituted α-In_2S_3. The density of states obtained from the HSE functional indicates formation of an empty IB, when one V ion—corresponding to a concentration of 1.9 at %—substitutes 16d octahedral lattice sites. Note that the formed IB does not show large electronic coupling between the vanadium ion and the host ions, though, and may thus induce some recombination despite not being strictly localised. By increasing the V concentration, the energy gap between the IB and the CB closes and the empty state overlaps with the CB and results in band gap reduction. A similar situation arises through incorporation of V ions on 8a tetrahedral sites for both low and high V concentration. This shows that the details of the electronic structure of In_2S_3:V depend on both the crystal structure and the V incorporation site. However, a partially filled IB, as required for solar cell application, is not formed in any of the studied cases.

Data availability statement

The data cannot be made publicly available upon publication because they are not available in a format that is sufficiently accessible or reusable by other researchers. The data that support the findings of this study are available upon reasonable request from the authors.

Acknowledgments

We acknowledge the ESRF and the CNR-IOM for provision of synchrotron radiation facilities (Experiment: MA-3671) and we thank Dr Giovanni Lepore and Dr Alessandro Puri for their valuable help during the beamtime at LISA (BM08). We also thank Dr Konrad Ritter and Dr Sven Schönherr for assistance with sample preparation and EDX measurements. E G would like to thank Deutsche Forschungsgemeinschaft (DFG) for the financial support through Project No. 414750661. The computing time was granted by the NHR4CES Resource Allocation Board and provided on the supercomputer Lichtenberg II at TU Darmstadt as part of the NHR4CES infrastructure. The calculations for this research were conducted with computing resources under the Project 01316. R S gratefully acknowledges the DFG funding through SCHE 1745/6-1.

Conflicts of interest

There are no conflicts of interest to declare.

ORCID iDs

Elaheh Ghorbani https://orcid.org/0000-0002-4037-1602
Hans H Falk https://orcid.org/0000-0002-9019-7614
Francesco d'Acapito https://orcid.org/0000-0003-2207-6113
Karsten Albe https://orcid.org/0000-0003-4669-8056
Claudia S Schnohr https://orcid.org/0000-0002-3688-7104

References

[1] Okada Y *et al* 2015 Intermediate band solar cells: recent progress and future directions *Appl. Phys. Rev.* **2** 48
[2] Ramiro I and Martí A 2020 Intermediate band solar cells: present and future *Prog. Photovolt.* **29** 705–13
[3] Luque A and Marti A 1997 Increasing the efficiency of ideal solar cells by photon induced transitions at intermediate levels *Phys. Rev. Lett.* **78** 5014
[4] Luque A and Marti A 2001 A metallic intermediate band high efficiency solar cell *Prog. Photovolt.* **9** 73
[5] Luque A, Marti A, Antolin E and Tablero C 2006 Intermediate bands versus levels in non-radiative recombination *Physica* B **382** 320
[6] Krich J J, Halperin B I and Aspuru-Guzik A 2012 Nonradiative lifetimes in intermediate band photovoltaics-absence of lifetime recovery *J. Appl. Phys.* **112** 013707
[7] Strandberg R and Aguilera I 2012 Evaluation of vanadium substituted In_2S_3 as a material for intermediate band solar cells *Sol. Energy Mat. Sol. Cells* **98** 88
[8] Palacios P, Aguilera I, Sanchez K, Conesa J C and Wahnon P 2008 Transition-metal-substituted indium thiospinels as novel intermediate-band materials: prediction and understanding of their electronic properties *Phys. Rev. Lett.* **101** 046403
[9] Pistor P, Alvarez J M M, Leon M, di Michiel M, Schorr S, Klenk R and Lehmann S 2016 Structure reinvestigation of alpha-, beta- and gamma-In_2S_3 *Acta Crystallogr.* B **72** 410
[10] Chen P, Chen H J, Qin M S, Yang C Y, Zhao W, Liu Y F, Zhang W Q and Huang F Q 2013 Fe-substituted indium thiospinels: new intermediate band semiconductors with better absorption of solar energy *J. Appl. Phys.* **113** 213509
[11] Lucena R, Aguilera I, Palacios P, Wahnon P and Conesa J C 2008 Synthesis and spectral properties of nanocrystalline V-substituted In_2S_3, a novel material for more efficient use of solar radiation *Chem. Mater.* **20** 5125
[12] Lucena R, Conesa J C, Aguilera I, Palacios P and Wahnon P 2014 V-substituted In_2S_3: an intermediate band material with photocatalytic activity in the whole visible light range *J. Mater. Chem.* A **2** 8236
[13] McCarthy R F, Weimer M S, Haasch R T, Schaller R D, Hock A S and Martinson A B F 2016 $V_xin_2 - xs_3$ intermediate band absorbers deposited by atomic layer deposition *Chem. Mater.* **28** 2033
[14] Tapia C *et al* 2016 Synthesis and characterization of V-doped beta-In_2S_3 thin films on FTO substrates *J. Phys. Chem.* C **120** 28753
[15] Waegele L A, Rata D, Gurieva G and Scheer R 2017 Structural analysis of co-evaporated In_2S_3 and In_2S_3:V for solar cell absorber applications *Phys. Status Solidi* c **14** 1600204
[16] Jawinski T, Waegele L A, Scheer R, Grundmann M and von Wenckstern H 2018 Properties of In_2S_3-based pin-heterojunctions *Phys. Status Solidi* a **215** 1700827
[17] Jawinski T, Lorenz M, Scheer R, Grundmann M and von Wenckstern H 2020 Properties of epitaxially grown In_2S_3:V thin films for intermediate band solar cell application *Proc. 47th IEEE Photovoltaic Specialists Conf. (PVSC, Calgary, 2020)* p 2663
[18] Ho C H 2011 Enhanced photoelectric-conversion yield in niobium-incorporated In_2S_3 with intermediate band *J. Mater. Chem.* **21** 10518
[19] Ghorbani E, Erhart P and Albe K 2019 New insights on the nature of impurity levels in V-doped In_2S_3: why is it impossible to obtain a metallic intermediate band? *J. Mater. Chem.* A **7** 7745

[20] Ghorbani E, Barragan-Yani D and Albe K 2020 Towards intermediate-band photovoltaic absorbers: theoretical insights on the incorporation of Ti and Nb in In_2S_3 *npj Comp. Mater.* **6** 93
[21] Mariyal Jebasty R, Olafsen SjÅstad A and Vidya R 2022 Prediction of intermediate band in Ti/V doped γ-In_2S_3 *RSC Adv.* **12** 1331
[22] Bensch W and Koy J 1993 Structure of hexagonal V_3S_4 determined at three different temperatures *Acta Crystallogr.* C **49** 1133
[23] Bensch W and Koy J 1993 The single crystal structure of V_5S_8 determined at two different temperatures: anisotropic changes of the metal atom network *Inorg. Chim. Acta* **206** 221
[24] Schnohr C S 2015 Compound semiconductor alloys: from atomic-scale structure to bandgap bowing *Appl. Phys. Rev.* **2** 031304
[25] Ritter K, Eckner S, Preiß C, Gurieva G, Bischoff T, Welter E, Botti S, Schorr S and Schnohr C S 2020 Atomic scale structure and its impact on the band gap energy for $Cu_2Zn(Sn,Ge)Se_4$ kesterite alloys *J. Phys.: Energy* **2** 035004
[26] Schöppe P *et al* 2020 Revealing the origin of the beneficial effect of cesium in highly efficient $Cu(In,Ga)Se_2$ solar cells *Nano Energy* **71** 104622
[27] Barreau N, Bernede J, Deudon C, Brohan L and Marsillac S 2002 Study of the new β-In_2S_3 containing Na thin films part I: synthesis and structural characterization of the material *J. Cryst. Growth* **241** 4–14
[28] Barreau N, Bernede J and Marsillac S 2002 Study of the new beta-In_2S_3 containing Na thin films. Part II: optical and electrical characterization of thin films *J. Cryst. Growth* **241** 51
[29] Barreau N, Bernede J, Marsillac S, Amory C and Shafarman W 2003 New Cd-free buffer layer deposited by PVD: In_2S_3 containing Na compounds *Thin Solid Films* **431** 326
[30] Ghorbani E and Albe K 2018 Influence of Cu and Na incorporation on the thermodynamic stability and electronic properties of β-In_2S_3 *J. Mater. Chem.* C **6** 7226
[31] d'Acapito F, Lepore G O, Puri A, Laloni A, La Manna F, Dettona E, De Luisa A and Martin A 2019 The LISA beamline at ESRF *J. Synchrotron Rad.* **26** 551
[32] Newville M 2001 IFEFFIT: interactive XAFS analysis and FEFF fitting *J. Synchrotron Rad.* **8** 322
[33] Ravel B and Newville M 2005 ATHENA, ARTEMIS, HEPHAESTUS: data analysis for x-ray absorption spectroscopy using IFEFFIT *J. Synchrotron Rad.* **12** 537
[34] Rehr J J, Kas J J, Vila F D, Prange M P and Jorissen K 2010 Parameter-free calculations of x-ray spectra with FEFF9 *Phys. Chem. Chem. Phys.* **12** 5503
[35] Haubold E, Schöppe P, Eckner S, Lehmann S, Colantoni I, d'Acapito F, di Benedetto F, Schorr S and Schnohr C S 2019 Short-range versus long-range structure in $Cu(In,Ga)Se_2$, $Cu(In,Ga)3Se_5$ and $Cu(In,Ga)5Se_8$ *J. Alloys Compd.* **774** 803
[36] Newville M 2005 Using bond valence sums as restraints in XAFS analysis *Phys. Scr.* **T115** 159
[37] Kresse G and Furthmueller J 1996 Efficient iterative schemes for *ab initio* total-energy calculations using a plane-wave basis set *Phys. Rev.* B **54** 11169
[38] Kresse G and Furthmueller J 1996 Efficiency of *ab-initio* total energy calculations for metals and semiconductors using a plane-wave basis set *Comput. Mater. Sci.* **6** 15
[39] Heyd J, Scuseria G E and Ernzerhof M 2003 Hybrid functionals based on a screened coulomb potential *J. Chem. Phys.* **118** 8207
[40] Ghorbani E and Albe K 2018b A hybrid functional view of intrinsic point defects in β-In_2S_3 *J. Appl. Phys.* **123** 103103
[41] Kresse G and Joubert D 1999 From ultrasoft pseudopotentials to the projector augmented-wave method *Phys. Rev.* B **59** 1758
[42] Bloechl P E 1994 Projector augmented-wave method *Phys. Rev.* B **50** 17953
[43] Glatzel P, Smolentsev G and Bunker G 2009 The electronic structure in 3d transition metal complexes: can we measure oxidation states? *J. Phys.: Conf. Series* **190** 012046
[44] Yamamoto T 2008 Assignment of pre-edge peaks in k-edge x-ray absorption spectra of 3d transition metal compounds: electric dipole or quadrupole? *X-Ray Spectrom.* **37** 5724
[45] Wong J, Lytle F W, Messmer R P and Maylotte D H 1984 K-edge absorption-spectra of selected vanadium compounds *Phys. Rev.* B **30** 5596